Mapping local field enhancements at nanostructured metal surfaces by second-harmonic generation induced in the near field

M. CELEBRANO*, M. ZAVELANI-ROSSI*, D. POLLI*,
G. CERULLO*, P. BIAGIONI†, M. FINAZZI†, L. DUÒ†,
M. LABARDI‡, M. ALLEGRINI‡, J. GRAND§ & P.-M. ADAM§

**ULTRAS-CNR-INFM, Physics Department, Politecnico di Milano, Piazza Leonardo da Vinci 32,
L-20133 Milan, Italy*

*†L-NESS, Physics Department, Politecnico di Milano, Piazza Leonardo da Vinci 32, L-20133,
Milan, Italy*

*‡Polylab CNR- INFM, Physics Department 'Enrico Fermi', University of Pisa, Largo Pontecorvo 3,
56127 Pisa, Italy*

*§LNIO, University of Technology of Troyes, 12 Rue Marie Curie, PO Box 2060, 10010 Troyes
Cedex, France*

Summary

We report on an aperture scanning near-field optical
microscope in which femtosecond pulses are coupled to a
hollow-pyramid aperture sensor. Such probe displays high
throughput and preserves pulse duration and polarization,
enabling the achievement of sufficiently high peak power in
the near field to perform nonlinear optics on the nanoscale.
We use the system to observe the nonlinear optical response
of nanostructured metal surfaces with sub-100-nm spatial
resolution. We study second-harmonic generation from gold
nanoparticles both isolated and in high-density patterns,
highlighting a strong dependence of the generation efficiency
on the shape and on the fine structure of the nanoemitter. In
particular, we present results on closely packed gold triangles as
well as on nanoellipsoids with different local surface plasmon
resonances.

Introduction

The rapid development of nanoscience and nanotechnology
during the last years has stimulated research on the analysis
of nanoscale electromagnetic fields, and the development of
tools for studying and exploiting them to obtain new compact
and all-optical devices (Barnes *et al.*, 2003; Bozhevolnyi *et al.*,
2006). One of the most remarkable effects in light interaction
with metal nanostructures is the strong (up to several orders of

magnitude) and spatially localized (on nanometre scale) field
intensity enhancement. This enhancement can occur because
of local coupling of light with particular resonant structures
(antenna effect) (Mühlschlegel *et al.*, 2005) or because of field
concentration on structures with strong curvature (lightning-
rod effect; Novotny & Stranick, 2006); another source of
huge field enhancements is the resonant excitation of the so-
called localized surface plasmons associated with individual
scatterers (Zayats & Smolyaninov, 2003). The resonance
frequencies of the localized surface plasmons can be tailored in
a broad spectral range according to the structure material and
shape. The nanoscale local field enhancement is best observed
exploiting nonlinear optical effects, such as second-harmonic
generation (SHG) (Smolyaninov *et al.*, 1997; Jakubczyk *et al.*,
1999; Smolyaninov *et al.*, 2000; Zayats *et al.*, 2000; Shen *et al.*,
2001) or two-photon photo-luminescence (Jakubczyk *et al.*,
1999; Bouhelier *et al.*, 2005; Imura *et al.*, 2006) which depend
on the square of the light intensity; to observe a significant
nonlinear response, the samples need to be illuminated by high
peak intensity femtosecond light pulses.

The nonlinear optical response of nanostructured surfaces
has been studied both theoretically (Dadap *et al.*, 1999;
Bozhevolnyi & Lozovski, 2002; Stockman *et al.*, 2004) and
experimentally by confocal optical microscopy (Bozhevolnyi
et al., 2003; Beermann & Bozhevolnyi, 2004). Far-field
techniques, however, are limited by diffraction and prevent
a direct mapping of nanoscale optical fields; moreover,
such techniques are not effective for investigating single
nanostructures in high-density arrangements. The scanning
near-field optical microscope (SNOM) allows overcoming the

Correspondence to: M. Zavelani-Rossi. Tel: +39 22399 6069; fax: +39 22399 6126;
e-mail: margherita.zavelani@fisi.polimi.it

diffraction limit by confining the light on the nanometre scale (Pohl *et al.*, 1984; Smolyaninov *et al.*, 1997; Zayats & Sandoghdar, 2000) providing simultaneously information on the sample topography. In this paper we describe a novel experimental setup in which femtosecond pulses are coupled to a hollow-pyramid aperture SNOM, enabling the achievement of sufficiently high peak power to perform nonlinear optics in the near field. We use such a system to observe the nonlinear optical response of tightly packed nanostructures with sub-100-nm spatial resolution, presenting results on SHG of single gold nanoparticles both in isolated and in high-density patterns. The paper is organized as follows: in section 'Materials and methods' we describe the experimental setup and the investigated samples; in section 'Results and discussion' we present results of SHG optical imaging; finally, in section 'Conclusions', we discuss performances versus limitations of our current setup and the envisaged improvements.

Materials and methods

Femtosecond laser system

A schematics of the laser system is shown in Fig. 1. It consists of a Ti:sapphire oscillator in an asymmetric cavity for Kerr-lens mode-locking. The cavity length is stretched by a 1:1 telescope (made of two $R = 2000$ mm mirrors) decreasing the repetition rate down to 26 MHz. For a given average power, as limited by thermal effects in the near-field probe, this allows an increase in the peak power by a factor of $\sim$4 with respect to a standard 100-MHz cavity, and a corresponding enhancement of nonlinear optical effects. The laser generates pulses at $\sim$800 nm central wavelength with 10 THz bandwidth (corresponding to a transform-limited pulse duration of 27 fs) and energy up to 20 nJ with an average power of $\sim$500 mW. The pulses are sent to a pre-compressor consisting of a double pass in a Brewster-cut fused-silica prism pair, then to a mechanical chopper with 1:6 duty cycle. The chopper on the one hand enables lock-in detection for stray light rejection, on the other hand it reduces the average power by a factor of 6 for a given peak power level, allowing an additional increase in nonlinear effects. The beam, passing through a half-wave plate used for polarization rotation, is then coupled to our homemade SNOM head.

Hollow-pyramid near-field probes

Standard aperture SNOMs are based on tapered optical fibres with nanometre-sized aperture tips confining the optical field into a sub-wavelength region. In order to acheive a spatial resolution comparable with the aperture size, the sample has to be kept at a distance from the apterture much smaller than the wavelength, enabling sample excitation with the evanescent component of the optical field (near-field). Typically, optical fibre tips have a metal coating with a small hole of the order of 50–100 nm. Such probes have a throughput in the range 10^{-6}–10^{-4n} and the input power is limited to 1–2 mW by thermal damage of the metal coating. The powers available at the tip output are therefore too low to enable the investigation
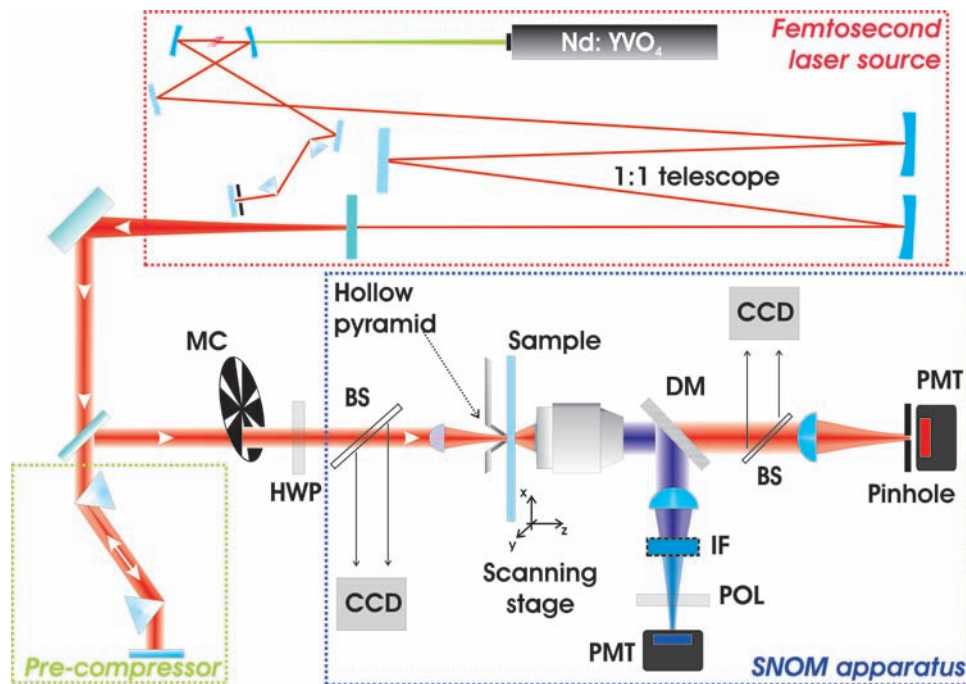
Fig. 1. Experimental setup of the nonlinear SNOM. CCD, camera for alignment; MC, mechanical chopper; HWP, half-wave plate; BS, beam splitter; DM, dichroic mirror; IF, interference filter; POL, polarizer; PMT, photomultiplier tube.

of nonlinear optical effects. In addition, pulse chirping because of propagation in the fibre leads to severe temporal broadening of ultrashort pulses, requiring pre-compensation techniques and preventing coupling of very short pulses.

Recently, a novel class of near-field aperture probes has been introduced (Werner *et al.*, 1998), based on silicon nitride cantilevers, similar to the ones used in atomic force microscopy (AFM), with a hollow pyramid as the tip. The pyramid is metal coated (usually by aluminium or gold) and a hole is produced at the pyramid apex, with diameter ranging from 60 to 200 nm. As shown in continuous-wave experiments, these cantilevered tips offer several advantages compared to metal-coated tapered optical fibres, namely: (i) the larger taper angle produces power throughputs higher by a factor of $\approx$10; (ii) the lower absorption allows coupling one order of magnitude higher average power before the onset of thermal damage. These improvements enable achieving two orders of magnitude higher power in the near field of the tip, resulting in greatly enhanced nonlinear optical response. In addition tip/sample distance stabilization methods used in AFM, such as the tapping mode, can be employed, ensuring longer probe lifetimes and sample preservation. Moreover light polarization is maintained in the near field of the aperture (Biagioni *et al.*, 2005) enabling polarization dependent experiments.

When used with femtosecond pulses, hollow pyramids offer the additional advantage of avoiding pulse lengthening because the pulses propagate through a very small optical thickness. In previous experiments (Labardi *et al.*, 2005) we characterized femtosecond pulses transmitted by these probes by second-order autocorrelation measurements. It was demonstrated that transmission through probes with diameter down to 65 nm has negligible effects on pulses with duration down to 30 fs, thus allowing simultaneous strong energy localization both in space and time.

Hollow-pyramid SNOM

Our SNOM setup is shown in Fig. 1. Ultrashort pulses from the pre-compressor are coupled to an aspheric lens (N.A. $\sim$0.5, completely filled) that is mounted on a three-axes piezo-translator (Nanocube, Physik Instrumente, GmbH & Co. KG, Karlsruhe, Germany) and focused into the hollow-pyramid cantilever probe (Witec GmbH, Ulm, Germany). The piezo-translators are needed to achieve the alignment accuracy required for efficient coupling to the tip. The numerical aperture of the lens is close to the taper angle of the pyramid, optimizing coupling efficiency. CCD cameras are used to image the back and the front sides of the pyramid to facilitate light coupling. The employed tips are made of silicon and coated with aluminium, and have an aperture varying between 100 and 200 nm. Throughputs at 800-nm excitation wavelength range from 10^{-4} for 100-nm apertures to 5×10^{-3} for 200-nm apertures in accordance with the expected scaling with the sixth power of aperture diameter.

Tip/sample distance stabilization is achieved through a standard AFM configuration measuring the cantilever deflection (sensitivity $\sim$0.4 nN/mV); to avoid sample degradation the tapping-mode technique is implemented (although tests in 'soft' contact-mode show no sample modification). The feedback loop is closed by a standard analogue controller which drives the z-axis of a xyz piezo-scanner stage (Physik Instrumente) on which the sample is mounted; the xy raster scan is then produced by driving the stage with a homemade software in Labview, and an ADC input/output board (National Instruments, Austin, TX, USA).

Light transmitted by the aperture is collected by a 0.75-NA achromatic microscope objective; the fundamental wavelength (FW) and the second harmonic (SH) are separated by a dichroic beam splitter and are simultaneously detected by two different photomultipliers (PMT, Mod. R7400U, Hamamatsu, Japan). A band pass interferential filter is inserted on the SH beam path to further reject the FW component and the two-photon photo-luminescence from the sample; an overall FW suppression of $\sim$10^{-11} is thus achieved. In the FW path stray light suppression is achieved by a focusing lens and a spatial filter with a 50-μm-diameter pinhole.

In our experiments we used high throughput apertures, with diameters larger than 150 nm, and input powers of 1–2 mW; under these conditions average power on the sample is less than 1 μW and the average intensity is $\sim$1 kW/cm^2. Tests on the system show no evidence of tip and sample damage for input powers below 5 mW. An integration time of 30–100 ms per point during the scan is sufficient to ensure a good signal-to-noise ratio.

Samples

We used two different types of nanostructured metal surfaces. The first is a commercial (Kentax GmbH, Seelze, Germany) metal latex projection pattern, also known as Fischer pattern (Fischer & Zingsheim, 1981) that was chosen as a test sample. It consists of approximately flat gold triangles, with $\sim$15 nm nominal height, faced tip to tip on a glass substrate, in a hexagonal arrangement with $\sim$453 nm periodicity. The second sample typology consists of square arrays of gold ellipsoids produced by electron beam lithography (Grand *et al.*, 2003). To achieve electron beam lithography, we operate a 30-kV Hitachi S-3500N scanning electron microscope (Hitachi Ltd, Tokyo, Japan) equipped with a nanometre pattern generation system (J. C. Nabity Lithography Systems, Bozeman, MT, USA). The structures are fabricated on a quartz substrate to suppress parasitic luminescence. A high-resolution polymethylmetacrylate resist is spin coated over the substrate and covered by 10 nm of aluminium. After exposure, the patterns are developed using methylisobutylketone:isopropyl alcohol (1:3) and the desired mass thickness of gold is evaporated on the sample. Lift-off is then performed using acetone. The short axis of the ellipsoids is
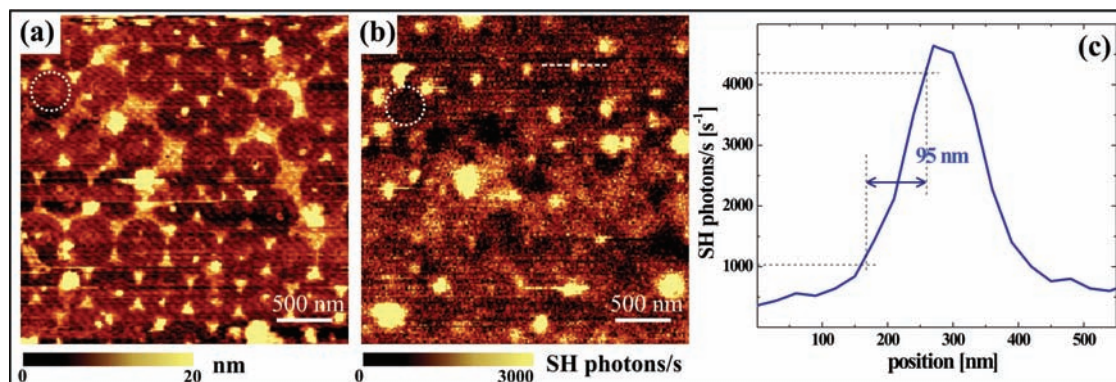
Fig. 2. SHG from gold projection pattern: (a) topographic image; (b) SHG image and (c) SHG profile. Scan area $3.5 \times 3.5 \mu m$.

~70 nm long, the long axis can be either 100, 150 or 400 nm long, the height is ~70 nm, and the array period is 1 μm.

Results and discussion

Figure 2a shows the topography of the Fischer pattern together with the SHG optical image (Fig. 2b), acquired with a 150-nm aperture tip. The lateral shift of the optical image with respect to the topographic image denotes that tip/sample stabilization resulted from a protrusion at one side of the aperture rim. The topography shows the regular array of Au triangles, whereas the FW image (not shown) is almost featureless, because of the quite large diameter of the aperture. Nevertheless, very strong and well-resolved SHG from the gold triangles is detected. The background signal is attributed to both the glass substrate and to SHG from the tip edges. There are also some larger spots in the optical image, coming from gold aggregates present in the sample, as it can be seen on the topographic map. The signal displays a very good signal-to-noise ratio and a remarkably good contrast. Defining the contrast as: $C = \frac{I_{np} - I_{sub}}{I_{sub}} [\%]$, where I_{np} is the light intensity collected on the nanoparticle and I_{sub} that of the substrate, we find C higher than 700%, as shown by the profile in Fig. 2(c). The optical resolution of the image, adopting the 10–90% criterion, is around 95 nm. The SHG image shows a resolution which is higher than the tip diameter, probably because of the multiphoton process together with the field enhancements localized at the aperture rims, as will be explained below. It is interesting to note that there is no 1:1 correspondence between the topography and the SHG image, because SH emission varies strongly from one triangle to the other. This is a direct proof of the absence of topographical artifacts. This conclusion is further confirmed by other measurements (not shown here) which show flat topography, due to the absence of sharp tip protrusions, but still preserve high resolution in the SHG maps. The strong variability of SHG efficiency at the triangles can be attributed to differences in local field enhancement, which are determined by the fine structure of the gold nanoemitters, e.g. related to the sharpness of triangles' apexes, not addressable

in our topographic image. Moreover, a comparison between topography and the optical map shows that most of the signals are collected when the tip is positioned above a single triangle, rather than at the centre of the gap of the bow-tie structures (Schuck *et al.*, 2005) that are formed by a couple of faced triangles. This is attributed to the local illumination mode used in our experimental setup, which probably does not allow efficient excitation of such resonant coupled structures.

Figure 3 summarizes the main properties of the gold nanoellipsoid samples. Figure 3a displays the topography of the nanoparticles and Figs 3(b) and (c) the far-field extinction spectra that are acquired exciting with light polarized along the major axis of the ellipsoids. Extinction spectra are recorded on a modified Jobin-Yvon confocal micro-Raman spectrometer; the sample is illuminated from the bottom side and the transmitted light is collected from a $70 \times 70 \mu m^2$ area by a $10\times$ microscope objective with 0.25 N.A. The 100-nm-long ellipsoids show a strong extinction peak at 690 nm, which shifts to 800 nm for the 150-nm-long ones. These peaks can be explained as due to surface plasmon resonances and correspond to theoretical expectations (Grand *et al.*, 2005).

The optical FW images and the corresponding SH images of some nanoellipsoids are displayed in Fig. 4. Figures 4(a) and (b) refer to the 100-nm-long particles whereas Figs 4(c) and (d) to the 150-nm ones. Incident light is polarized parallel to the long axes of the ellipsoids (horizontal in Fig. 4). FW images of particles with different length give opposite contrast: short ellipsoids appear bright because of the scattering of incident light, whereas longer particles appear dark, probably because of light absorption. This shows that the short particles are out of resonance whereas the longer ones are resonant with the 800-nm excitation, in agreement with far-field extinction spectra. The SH images also display a strong dependence on the ellipsoid length: Short particles are hardly distinguishable because they do not emit SH, whereas 150-nm-long particles show a high SH emission with remarkable contrast ($C = 110\%$). The lack of SHG from one particle in Fig. 4(b) can be attributed to fabrication imperfections and gives further evidence of the sensitivity of nonlinear processes to
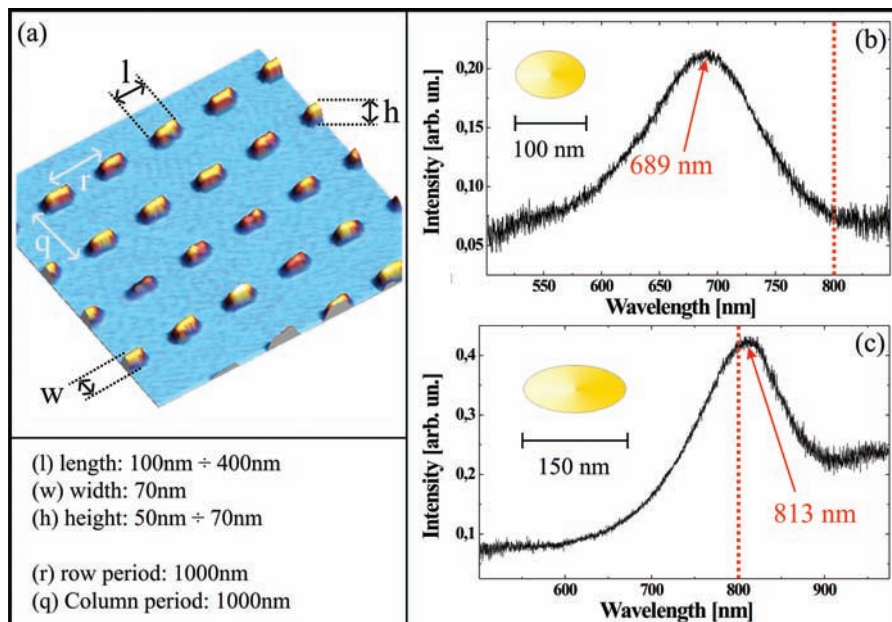
Fig. 3. Characteristics of the gold nanoellipsoids with length varying from 100 to 400 nm. (a) 3D AFM image of 400-nm-long particles acquired with the hollow-pyramid near-field probe. (b) and (c) far field extinction spectra of 100-nm- and 150-nm-long particles, respectively. Dashed red line corresponds to femtosecond laser excitation wavelength.
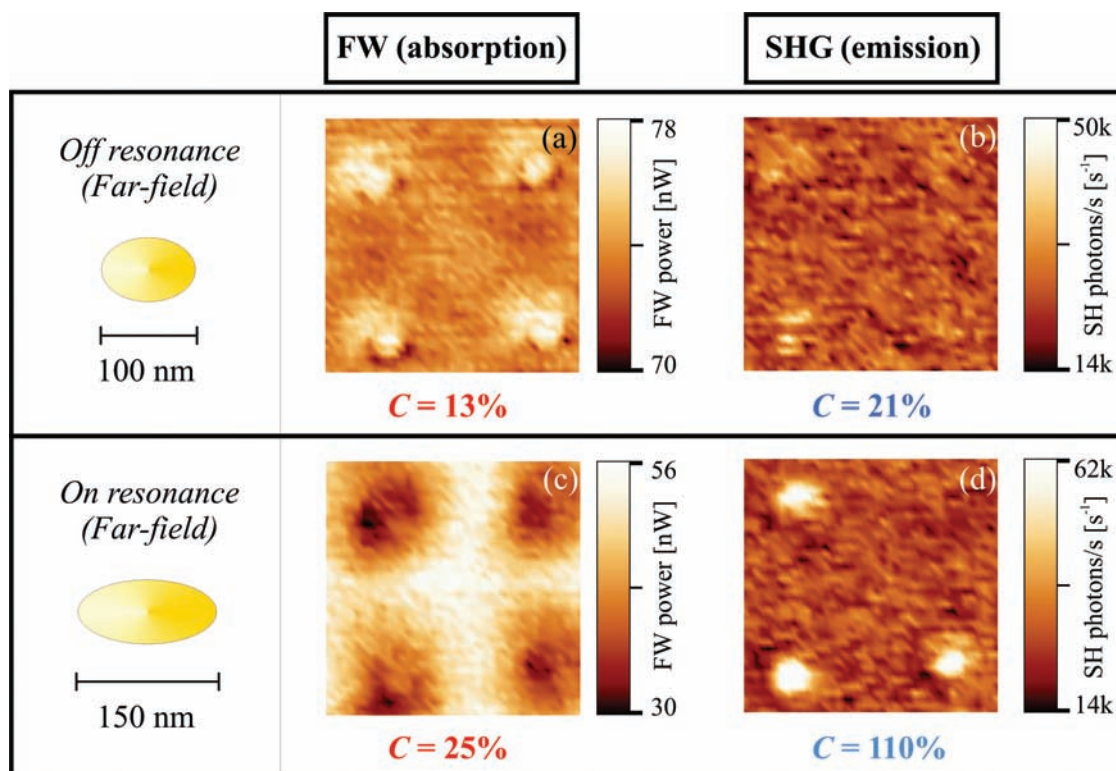

Fig. 4. (a) FW image of 100-nm-long nanoparticles and (b) corresponding SHG image. (c) FW image of 150-nm-long nanoparticles and (d) corresponding SHG image. Scan areas: $1.5 \times 1.5 \ \mu m^2$.
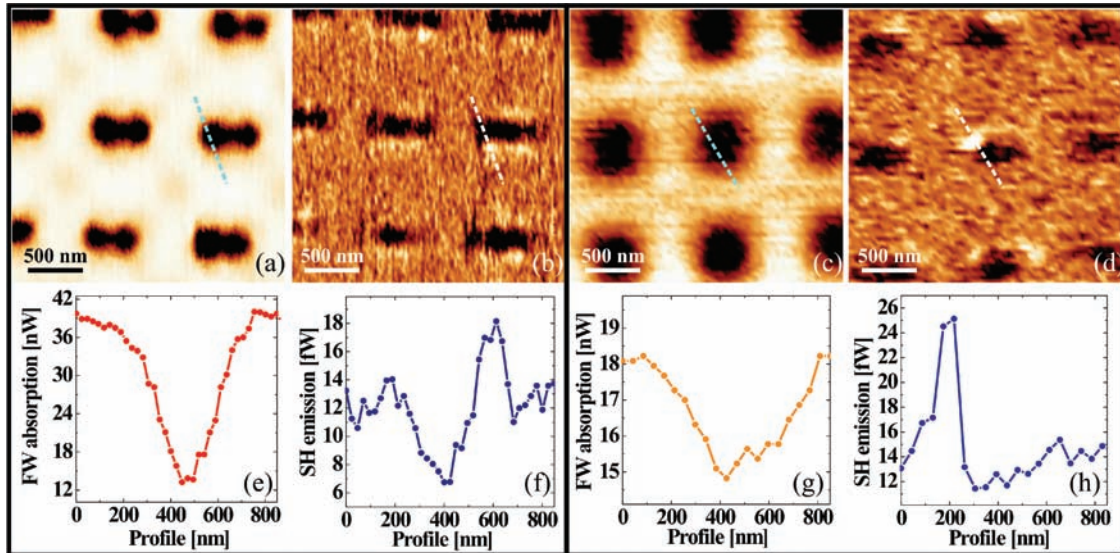
Fig. 5. Comparative images of 400-nm-long particle. (a) and (b) are, respectively, FW and SH images taken with ≈90-nm-tip aperture. (c) and (d) taken with a larger tip. Scan areas are 2.5 × 2.5 μm wide; the first two are composed of 128 × 128 pixels, the latter two have half pixels. (e), (f), (g) and (h) line profiles of corresponding upper images.

local morphology. Despite the poor spatial resolution of FW absorption images, the SH image in Fig. 4(d) shows again an unexpectedly high resolution (<100 nm).

Nano-ellispoids with 400-nm major axis are expected to be out of resonance. Figure 5 displays the FW and the SHG images of these particles. The relatively strong absorption of the FW light (Figs 5a and c) is because of its bulky structure with respect to the tip dimension, shadowing the aperture emission. SHG in Figs 5(b) and (d) is attributed to local imperfections along the border of the particles and to field enhancements owing to the locally small radius of curvature. Dark regions correspond to absorption of the SHG coming from the tip edges and this confirms the hypothesis of bulk behaviour.

An interesting feature of the nonlinear SNOM can be pointed out by observing Fig. 5. Figures 5(a) and (b) are acquired with a brand new tip (aperture of ∼100 nm and throughput of ∼10^{-4}) whereas Figs 5(c) and (d) are obtained after a great number of scans. The wear-induced increase of the aperture size is evident from the dramatic decrease of resolution in the FW images. Eventually the tip has doubled its diameter (throughput ∼5×10^{-3}). It is interesting to note that the SHG has preserved its original resolution. The profiles (Figs 5e–h)) show clearly the tip broadening and the resolution achieved. We can thus conclude that the resolution of SHG is not directly related to the aperture dimension; rather, we believe that the higher resolution observed in the SH images, which goes beyond the factor of $\sqrt{2}$ expected between SH and FW intensity distributions, could be ascribed to a tip-on-aperture-like field enhancement mechanism (Frey *et al.*, 2002), where the role of the aperture is to convey energy to a sharp protrusion or to a

sharp bend at the rim of the metal coating that acts as a near-field scattering centre. Field enhancements due to this effect can be observed only in the SH images, which are essentially background-free, with respect to the FW ones that reflect the interaction with the total amount of light transmitted by the aperture. Such mechanism is consistent with the fact that the high resolution in the SH image (<100 nm) is maintained even with the largest apertures (∼200 nm).

Conclusions

In this paper we have presented an aperture SNOM based on femtosecond light pulses coupled to a hollow-pyramid aperture probe; this instrument enables to achieve sufficient peak power in the near field to perform nonlinear optics on the nanoscale. The system allows obtaining SHG from single nanostructures in closely packed arrangements with very high resolution (down to 90 nm) and very high optical contrast (up to ∼800%), enabling researchers to characterize the local field enhancements arising from metallic nanoparticles on the nanometre scale.

The performances of the system can be improved by using smaller tips, hence increasing resolution. This would imply a reduction of the SHG signal; nevertheless, it would be possible to increase the detection sensitivity by photon counting detection and/or more sensitive detectors, such as a single photon avalanche photodiode. It would be also possible to increase the peak power at the tip apex at a given level of average power below tip damage threshold by decreasing the chopper duty-cycle or implementing a pulse picker on the laser beam. Finally, we are presently testing a new promising generation of

hollow-pyramid cantilever sensors which preserves resolution while increasing throughput values.

Acknowledgements

References

Barnes, W.L., Dereux, A. & Ebbesen, T.W. (2003) Surface plasmon subwavelength optics. *Nature* **424**, 824–830.

Beermann, J. & Bozhevolnyi, S.I. (2004) Microscopy of localized second-harmonic enhancement in random metal nanostructures. *Phys. Rev. B* **69**, 155429-1-9.

Biagioni, P., Polli, D., Labardi, M., *et al.* (2005) Unexpected polarization behavior at the aperture of hollow-pyramid near-field probes. *Appl. Phys. Lett.* **87**, 223112-1-3

Bouhelier, A., Bachelot, R., Lerondel, G., Kostcheev, S., Royer, P. & Wiederrecht, G.P. (2005) Surface plasmon characteristics of tunable photoluminescence in single gold nanorods. *Phys. Rev. Lett.* **95**, 267405-1-4.

Bozhevolnyi, S.I. & Lozovski, V.Z. (2002) Second-harmonic scanning optical microscopy of individual nanostructures. *Phys Rev B* **65**, 235420-1-10.

Bozhevolnyi, S.I., Beermann, J. & Coello, V. (2003) Direct observation of localized second harmonic enhancement in random metal nanostructures. *Phys. Rev. Lett.* **90**, 197403-1-4.

Bozhevolnyi, S.I., Volkov, V.S., Devaux, E., Laluet, J.-Y. & Ebbesen, T.W. (2006) Channel plasmon subwavelength waveguide components including interferometers and ring resonators. *Nature* **440**, 508–511.

Dadap, J.I., Shan, J., Eisenthal, K.B. & Heinz, T.F. (1999) Second-harmonic Rayleigh scattering from a sphere of centrosymmetric material. *Phys. Rev. Lett.* **83**, 4045–4048.

Fischer, U. Ch. & Zingsheim, H.P. (1981) Submicroscopic pattern replication with visible light. *J. Vac. Sci. Technol. B* **19**, 881–885.

Frey, H.G., Keilmann, F., Kriele, A. & Guckenberger, R. (2002) Enhancing the resolution of scanning near-field optical microscopy by a metal tip grown on an aperture probe. *Appl. Phys. Lett.* **81**, 5030–5032.

Grand, J., Kostcheev, S., Bijeon, J.-L., *et al.* (2003) Optimization of SERS-active substrates for near-field raman spectroscopy. *Synth. Met.* **139**, 621–624.

Grand, J., Lamy de la Chapelle, M., Bijeon, J.-L., Adam, P.-M., Vial, A. & Royer, P. (2005) Role of localized surface plasmons in surface-enhanced Raman scattering of shape-controlled metallic particles in regular arrays. *Phys. Rev. B* **72**, 033407-1-4.

Imura, K., Nagahara, T. & Okamoto, H. (2006) Photoluminescence from gold nanoplates induced by near-field two-photon absorption. *Appl. Phys. Lett.* **88**, 023104-1-3.

Jakubczyk, D., Shen, Y., Lal, M., Kim, K.S., Świtkewicz, J. & Prasad, P.N. (1999) Near-field probing of nanoscale nonlinear optical processes. *Opt. Lett.* **24**, 1151–1153.

Labardi, M., Zavelani-Rossi, M., Polli, D., Cerullo, G., Allegrini, M., De Silvestri, S. & Svelto, O. (2005) Characterization of femtosecond light pulses coupled to hollow-pyramid near-field probes: Localization in space and time. *Appl. Phys. Lett.* **86**, 031105-1-3.

Mühlschlegel, P., Eisler, H.-J., Martin, O.J.F., Hecht, B. & Pohl, D.W. (2005) Resonant optical antennas. *Science* **308**, 1607–1609.

Novotny, L. & Stranick, S.J. (2006) Near-field optical microscopy and spectroscopy with pointed probes. *Annu. Rev. Phys. Chem.* **57**, 303–331.

Pohl, D. W., Denk, W. & Lanz, M. (1984) Optical stethoscopy: Image recording with resolution l/20. *Appl. Phys Lett.* **44**, 651–653.

Schuck, P.J., Fromm, D.P., Sundaramurthy, A., Kino, G.S. & Moerner, W.E. (2005) Improving the mismatch between light and nanoscale objects with gold bowtie nanoantennas. *Phys. Rev. Lett.* **94**, 017402-1-4.

Shen, Y., Markowicz, P., Winiarz, J., Swiatkiewicz, J. & Prasad, P.N. (2001) Nanoscopic study of second-harmonic generation in organic crystals with collection-mode near-field scanning optical microscopy. *Opt. Lett.* **26**, 725–726.

Smolyaninov, I.I., Zayats, A.V., Davis, C.C. (1997) Near-field second-harmonic generation from a rough metal surface. *Phys. Rev. B* **56**, 9290–9293.

Smolyaninov, I.I., Liang, H.Y., Lee, C.H., Davis, C.C., Aggarwal, S. & Ramesh, R. (2000) Near-field second-harmonic microscopy of thin ferroelectric films. *Opt. Lett.* **25**, 835–837.

Stockman, M.I., Bergman, D.J., Anceau, C., Brasselet, S. & Zyss, J. (2004) Enhanced second harmonic generation by metal surfaces with nanoscale roughness: Nanoscale dephasing, depolarization, and correlations. *Phys. Rev. Lett.* **92**, 057402-1-4.

Werner, S., Rudow, O., Mihalcea, C. & Oesterschulze, E. (1998) Cantilever probes with aperture tips for polarization-sensitive scanning near-field optical microscopy. *Appl. Phys. A* **66**, S367–S370.

Zayats, A.V. & Sandoghdar, V. (2000) Apertureless scanning near-field second-harmonic microscopy. *Opt. Commun.*, **178**, 245–249.

Zayats, A.V. & Smolyaninov, I.I. (2003) Near-field photonics: Surface plasmon polaritons and localised surface plasmons. *J. Opt. A: Pure Appl. Opt.* **5**, S16–S50.

Zayats, A.V., Sandoghdar, V., Kalkbrenner, T. & Mlynek, J. (2000) Second-harmonic generation from individual surface defects under local excitation. *Phys. Rev. B* **61**, 4545–4548.